Project No: 603502

DACCIWA

"Dynamics-aerosol-chemistry-cloud interactions in West Africa"

Deliverable

D6.5 Model evaluation

<u>**Due date of deliverable:**</u>	30/11/2018
<u>**Completion date of deliverable:**</u>	18/12/2018

Start date of DACCIWA project:	1st December 2013	**Project duration:**	60 months

Version:	[V1.0]
File name:	[D6.5_Model_evaluation_DACCIWA_v1.0.pdf]

Work Package Number:	**6**
Task Number:	**5**

<u>**Responsible partner for deliverable:**</u>	**UPS**
Contributing partners:	**KIT**

Project coordinator name:	Prof. Dr. Peter Knippertz
Project coordinator organisation name:	Karlsruher Institut für Technologie

Dissemination level		
PU	Public	**x**
PP	Restricted to other programme participants (including the Commission Services)	
RE	Restricted to a group specified by the consortium (including the Commission Services)	
CO	Confidential, only for members of the consortium (including the Commission Services)	

Nature of Deliverable		
R	Report	**x**
P	Prototype	
D	Demonstrator	
O	Other	

Copyright

DOCUMENT INFO

Authors

Author	Beneficiary Short Name	E-Mail
Irene Reinares Martinez	UPS	irene.reinares@aero.obs-mip.fr
Jean-Pierre Chaboureau	UPS	jean-pierre.chaboureau@aero.obs-mip.fr
Andreas H. Fink	KIT	andreas.fink@kit.edu
Marlon Maranan	KIT	marlon.maranan@kit.edu
Jan Handwerker	KIT	jan.handwerker@kit.edu
Anke Kniffka	KIT	anke.kniffka@kit.edu

Changes with respect to the DoW

Issue	Comments
Only one proper warm rain events affected the Savè supersite and could be studied	Data from the X-band radar are indispensable to validate model runs. Thus, we were constrained to warm rain events in Savè.

Dissemination and uptake

Target group addressed	Project internal / external
Scientific community/Operational weather services	Internal and external

Document Control

Document version #	Date	Changes Made/Comments
V0.1	13.11.2018	First version drafted by UPS
V0.2	23.11.2018	Version including input by KIT for approval by the General Assembly
V1.0	18.12.2018	Final version approved by the General Assembly

Table of Contents

1   Introduction

Rainfall types over West Africa range from shallow, "warm-rain"-producing cloud elements to large organized, self-sustaining systems termed mesoscale convective systems (MCSs). While it is now commonly known that MCSs account for the vast majority of rainfall in the Sahel, there is a lack of robust rainfall type statistics for the wetter and more populous region of southern West Africa (SWA) lying to the south of the Sahel. Among them, warm rain formed by clouds composed only of liquid hydrometeors has been understudied in the past. However, some recent efforts have been undertaken to shed more light on the distribution and regional importance of warm rain. Using a five-year dataset from the Cloud-Aerosol Lidar with Orthogonal Polarization (CALIOP), Mülmenstädt et al. (2015) found generally a low probability of rain from warm clouds, which, however, increases towards coastal areas such as SWA. Based on a 16-year sample from the spaceborne Tropical Rainfall Measuring Mission (TRMM) precipitation radar, Maranan et al. (2018) estimated that warm rain contributes at least 2% to total annual rainfall at the immediate coastal region of SWA and that such warm rain events predominantly occur in July and August. Finally, Young et al. (2018) developed a SWA-calibrated method to delineate precipitating liquid clouds using the spatio-temporally high-resolution dataset of the Spinning Enhanced Visible and Infrared Imager (SEVIRI). They found a unimodal seasonal cycle of the occurrence frequency with a distinct peak in August, which corresponds well with the results in Maranan et al. (2018). Despite the likely small contribution to annual amounts, the contribution to precipitation frequency yielded by warm rain is larger and thus important for agriculture, in particular during the "little dry season", observed from mid-July to mid-September along the coast, sometimes associated with droughts (Adejuwon and Odekunle 2006). This motivates a better understanding of warm rain events.

Warm rain is typically produced by shallow clouds of small size. Current operational numerical-weather prediction models and convection-permitting research models run with grid meshes in the range of 1–20 km. The development of the boundary layer and the transition from stratus to convective clouds is at best partly resolved by these models, but usually fully parameterized. Thus, their ability to represent warm rain is likely limited. Large-Eddy Simulations (LESs) with grid spacing of 200 m or less can explicitly resolve the most energetic eddies in the boundary layer. Therefore, they are expected to better represent the warm rain processes.

The aim of this deliverable is to report on the model representation of warm rain processes in current models and their sensitivity to resolution and parameterization. A multi-model assessment is made for a warm rain event observed during the DACCIWA field campaign. It involves the operational forecast from the European Centre for Medium-Range Weather Forecasts (ECMWF) Integrated Forecast System (IFS), and simulations from two research models, ICON and Meso-NH, run at the kilometre scale. In addition, an LES run was performed with Meso-NH with a 200 m horizontal grid. The impact of resolution on precipitation amounts is investigated here and compared with ground-based radar observations.

The warm event was selected based on observations made at Savè in order to take advantage of the X-band radar of the Karlsruhe Institute of Technology (KIT). Indeed, the Savè supersite is the only DACCIWA supersite instrumented with rainfall radar (Kalthoff et al. 2018). During the aircraft campaign, no event was detected and outside this period, only one notable warm rain event was found on 24 July 2016. This case is analyzed based on the rain radar information and radiosonde observations.

This report is structured as follows: Section 2 presents the case study that was chosen for the model assessment. Section 3 contains a description of the models used (Meso-NH, ICON and IFS) and the observational datasets employed to assess the models. In Section 4, details on the evaluation

approach are given. In Section 5, the results of the multi-model assessment are presented. Section 6 presents more in-depth results for the Meso-NH LES and Section 7 concludes the report.

2   Case study of 24 July 2016

The vertical structure of clouds over Savè on the 24 July 2016 is shown in Figure 1. From 0300 to 0800 UTC large reflectivities, up to 15 dBZ, are observed below 2–3 km high. These shallow clouds occurring during the night and in the early morning are responsible for the warm rain observed by the distrometer (Figure 2). Deep convective clouds develop in the afternoon and evening, reaching 8–10 km before 2100 UTC and up to 12 km after 2100 UTC.
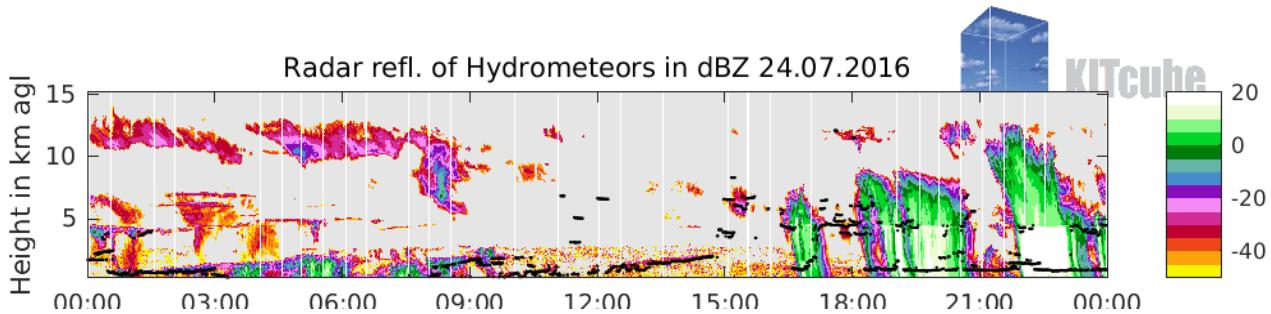
Figure 1: *Time evolution of the reflectivity measured in dBZ in the atmospheric column above Savè by the cloud radar deployed by the KIT.*
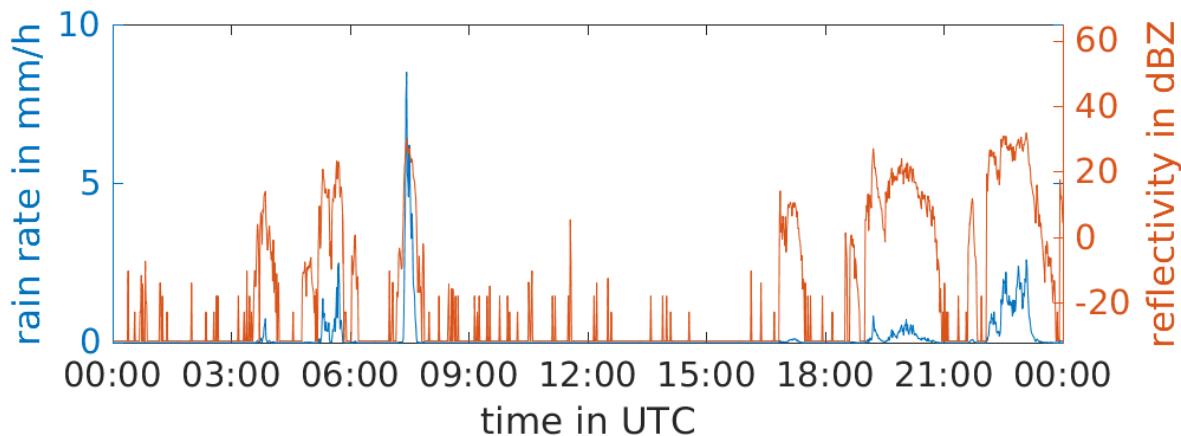
Figure 2: *Time evolution of the derived rain rate and radar reflectivity measured by a Joss-Waldvogel-Distrometer deployed by the KIT at Savè.*

Figure 3 presents the reflectivities retrieved by the X-band rain radar at 0530 UTC. Large amounts of precipitating hydrometeors are observed around Savè, with very low cloud tops. This vertical extension agrees with the cloud radar retrieval at that time (as shown in Figure 1). Other rain cells are observed around Savè. Those with tops below 4-5 km, composed of liquid hydrometeors, correspond to warm rain.
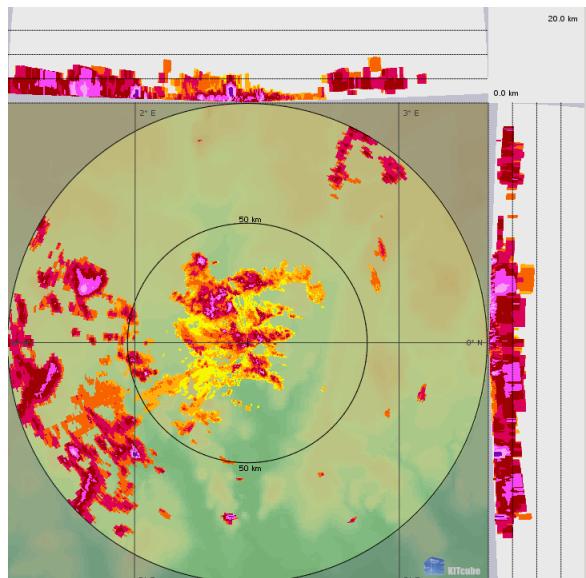
Figure 3: *X-band radar observations on 24 July 2016 0530 UTC. Shown are the horizontal (the outer circle represents the 100-km radar range) and the vertical projections (altitude vs. longitude and altitude vs. latitude) of the maximum reflectivity in dBZ.*

The 24 July 2016 is the only noticeable warm rain case found in Savè during the DACCIWA campaign period. Our idea is to take advantage of the high-frequency retrievals of the X-band radar (which scans at a 5-min frequency), as this allows the analysis of the fine scale processes involved in warm clouds and their rainfall. Given that the 24 July 2016 was an Intensive Operation Period (IOP), more frequent radiosoundings are available than for no-IOP days**.**

3 Models and observations

3.1 Models

3.1.1 Meso-NH

0.1.1

Two simulations, SAVKM and SAV02, were run with the non-hydrostatic mesoscale atmospheric Méso-NH model (Lac et al. 2018) with two nested grids over the domains centred over Benin (Figure 4) using a one-way nesting method (Stein et al. 2000). They share the same vertical grid. SAVKM was run for 18 h with a 1-km horizontal grid, and covers a domain of 1024x1024 km^2. It started from ECMWF operational analysis at 1800 UTC 23 July. Boundary conditions were provided by ECMWF operational analysis at 0000, 0600 and 1200 UTC 24 July. SAV02 was run for 10 h with a 200-m horizontal grid over a domain of 240x240 km^2, starting from SAVKM fields at 0200 UTC 24 July. Outputs were archived every 30 min for SAVKM and every 5 min for SAV02.

Both runs use the Surface Externalisée (SURFEX) scheme for surface fluxes (Masson et al. 2013), a microphysical scheme for mixed-phase clouds (Pinty and Jabouille 1998), and the Rapid Radiative Transfer Model (Mlawer et al. 1997) for longwave radiation and the two-stream scheme (Fouquart and Bonnel 1986) for shortwave radiation. The 3D turbulence scheme employed is a 1.5-order closure scheme (Cuxart et al. 2000) with the mixing length being the cubic root of the grid volume. A parameterization of dry thermals and shallow cumuli (Pergaud et al. 2009) is activated for SAVKM while no shallow convection parameterization is used for SAV02.
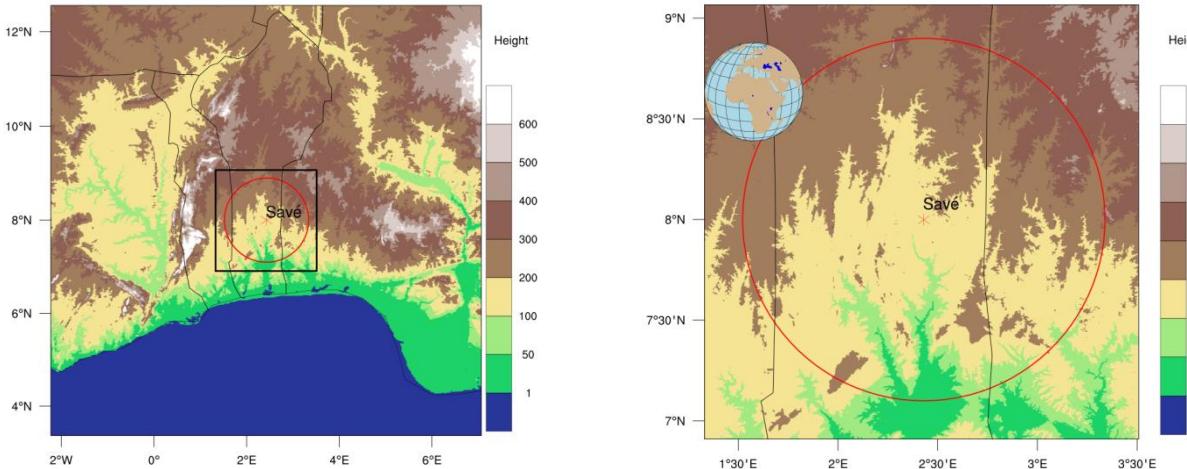
Figure 4: *Meso-NH simulation domains for SAVKM (left) and SAV02 (right). Colour-shaded is the terrain height. The black square in SAVKM represents the domain used in SAV02. The red circle shows the 100-km range of the X-band radar located at Savè.*

A third simulation SAVXX initialized at 0000 UTC 24 July 2016 is assessed in order to examine the sensitivity of the Meso-NH model to the initial conditions. SAVXX was run using the same set-up than the seven Meso-NH simulations described in Section 2 of Deliverable D6.4. In other words, it was run with a similar configuration than SAVKM, but with a horizontal grid spacing of 3 km instead of 1 km and over a smaller domain (see Deliverable D6.4).

3.1.2 IFS

IFS products were obtained from the ECMWF operational forecast starting at 0000 UTC 24 July 2016. We use 2D fields of total and convection precipitation, and 3D fields of temperature, horizontal components of the wind, specific humidity and specific content of cloud liquid water, cloud ice water, rain water and snow water at model levels. Thus, precipitating and non-precipitating hydrometeors can be distinguished. These products are available every 1 h and on a grid of 0.125° by 0.125°.

3.1.3 ICON

The ICON simulation was performed with two-nested models, one over the globe with a 13.2 km ICON-specific triangular grid and a nest over North Africa with 6.6 km horizontal resolution (Kniffka et al. 2018). For the latter resolution, the deep and shallow convection scheme was switched off. The simulation was initialized with ECMWF operational analysis at 1200 UTC 23 July. We use 2D fields of total precipitation, and 3D fields of temperature, horizontal wind speed, relative humidity and specific liquid water and ice water content. The water content in the atmosphere is not separated by hydrometeor type, only by phase. This means it is not possible to distinguish precipitating and non-precipitating hydrometeors. The ICON fields are available to us every 3 h and on a grid of 0.2° by 0.2° over a domain covering 8°W–8°E and 5°–10°N.

3.2 Observations

The rain gauge at Savè recorded 4.9 mm between 0600 UTC 23 July and 0600 UTC 24 July while the distrometer reported rain rates of less than 1 mm/h around 0900 and 1030 UTC. In addition to this observation of rain over Savè, we use satellite rainfall products, X-band radar reflectivity and radiosondes launched from Savè.

3.2.1 Radiosonde observations

During the DACCIWA campaign in June–July 2016, once-daily normal radiosonde observations are available at 0600 UTC, delivering profiles of the atmosphere up to ~20 km; and of additional high

frequency boundary layer soundings during the IOPs (Flamant et al., 2018). For this report, we use the standard observation on 24 July at 0600 UTC and two frequent observations at 0330 and 0800 UTC.

3.2.2 X-band radar reflectivity

The X-band radar installed at Savè during the DACCIWA field campaign (Kalthoff et al. 2018) has a frequency of 9.37 GHz, or equivalently a wavelength of ~3 cm. Its horizontal range is 100 km. The reflectivity data is available in a polar grid with a resolution of 500 m in the radial direction, of 1º in the azimuth angle for 12 elevation angles ranging from 0.69º to 90º. The whole volume is scanned every 5 min.

3.2.3 Satellite rainfall products

Two satellite products for rainfall are used in this report, to assess the simulations: the TRMM product 3B42, with a grid of 0.25ºx0.25º and a 3-hourly resolution (Huffman et al., 2007); and the Global Precipitation Mission (GPM) IMERG product with spatial and temporal resolution of 8 km and 30 min (Huffman et al., 2015).

4 Evaluation approach

The model assessment (Section 5) is performed over a common domain around Savè. The latter corresponds to the domain of the SAV02 simulation (Figure 4 right). The simulated rainfall is assessed against the TRMM 3B42 and GPM IMERG products from 0300 to 0900 UTC. This period is a bit longer than the interval when warm rain was observed in Savè in order to include three ICON outputs.

The contribution of warm rain to total rainfall is then estimated for the four simulations. To determine the presence of warm rain, it is needed to determine whether the precipitating hydrometeors are liquid. Here, we impose the bulk of the precipitating hydrometeors (mixing ratio larger than 0.1 g/kg) to be found below the melting layer (chosen here to be the 600-hPa level for an easy inter-model comparison) for ground precipitation to be warm rain. Only a negligible content of precipitating hydrometeors (mixing ratio lower than 0.1 g/kg) is allowed to be above the melting layer.

Both Meso-NH and IFS predict precipitating and non-precipitating hydrometeors, and the method explained above is straightforward. On the contrary, ICON predicts only two types of hydrometeors that are distinguished by phase, either liquid or solid. In order to determine whether a part of the hydrometeor predicted by ICON is precipitating or not, some thresholds are applied to the predicted liquid and ice water contents. These thresholds are taken equal to the autoconversion rates of liquid-to-rain and ice-to-snow of the microphysical scheme of Pinty and Jabouille (1998) used in the Meso-NH model. They are set to 0.5 g/m^3 for liquid and 2 10^{-5} kg/kg for ice. (These thresholds are somehow arbitrary and further investigation on the sensitivity of the results are needed.) Whenever the atmosphere is saturated and the liquid and ice contents are larger than those thresholds, the surplus is considered to be precipitating. Otherwise, in the case of an undersaturated atmosphere, the liquid and ice water contents are considered to be precipitating.

Finally, the simulated vertical structure of the atmosphere is evaluated. The vertical profiles of temperature, relative humidity and wind simulated at the gridpoint which is closest to Savè are compared against the data provided by the radiosondes.

For the LES assessment, we also take advantage of the 5-min temporal resolution of the radar to follow the warm rain cells both in the radar observations and the LES. To identify the warm rain cells, we used the clustering method developed by Reinares Martínez and Chaboureau (2018a). This method consists of locating the grid points where a condition is verified, and grouping those that are contiguous. We applied a mask on the intensity of the reflectivity (more than 20 dBZ as in Machado and Chaboureau, 2015) and their maximum altitude (less than 4 km) to locate the warm rain cells from radar and model data. We considered that this 4-km altitude corresponds to the freezing point temperature of 273 K in the clouds, which, for instance, is also roughly the same height that was used within TRMM to identify warm rain clouds in the tropics (Houze et al., 2015). All the higher, thus colder, clouds cannot produce warm rain. Notwithstanding, in the clouds, it is very common to find supercooled water. Thus glaciation phenomena frequently occur at temperatures below the melting temperature. In the absence of sufficiently precise data on this phenomenon, we decided to keep 4-km altitude threshold for warm rain being aware of the limitation of this choice. The clustering algorithm is then used to monitor the time evolution of the number of cells and to make 2-dimensional maps with rain cells as objects. As an example, Figure 5 shows a map of the 28 warm rain cells detected at 0530 UTC.
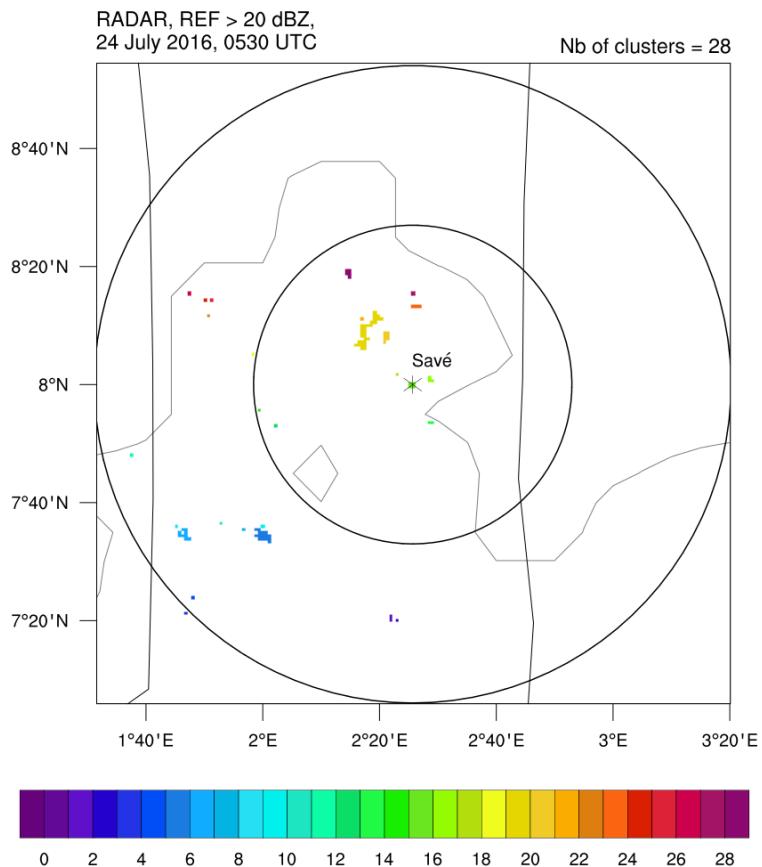
Figure 5: *Example of warm rain cells (top below 4-km height) identification from the X-band radar observations at 0530 UTC 24 July 2016, shown in Figure 3. The colours indicate the label number of each rain cell.*

5   Model assessment

5.1   Total rainfall

The accumulated rainfall from 0300 to 0900 UTC 24 July is shown for the two satellite products and the different simulations in Figure 6. Over Togo, the two satellite products both retrieved a rainfall area of 3 to 10 mm. Over Benin and Nigeria, TRMM indicates the absence of rainfall while GPM shows two 1-mm rainfall strips, among which is one over Savè. As a consequence, we cannot use any of the satellite rainfall products as a reference for the model assessment.
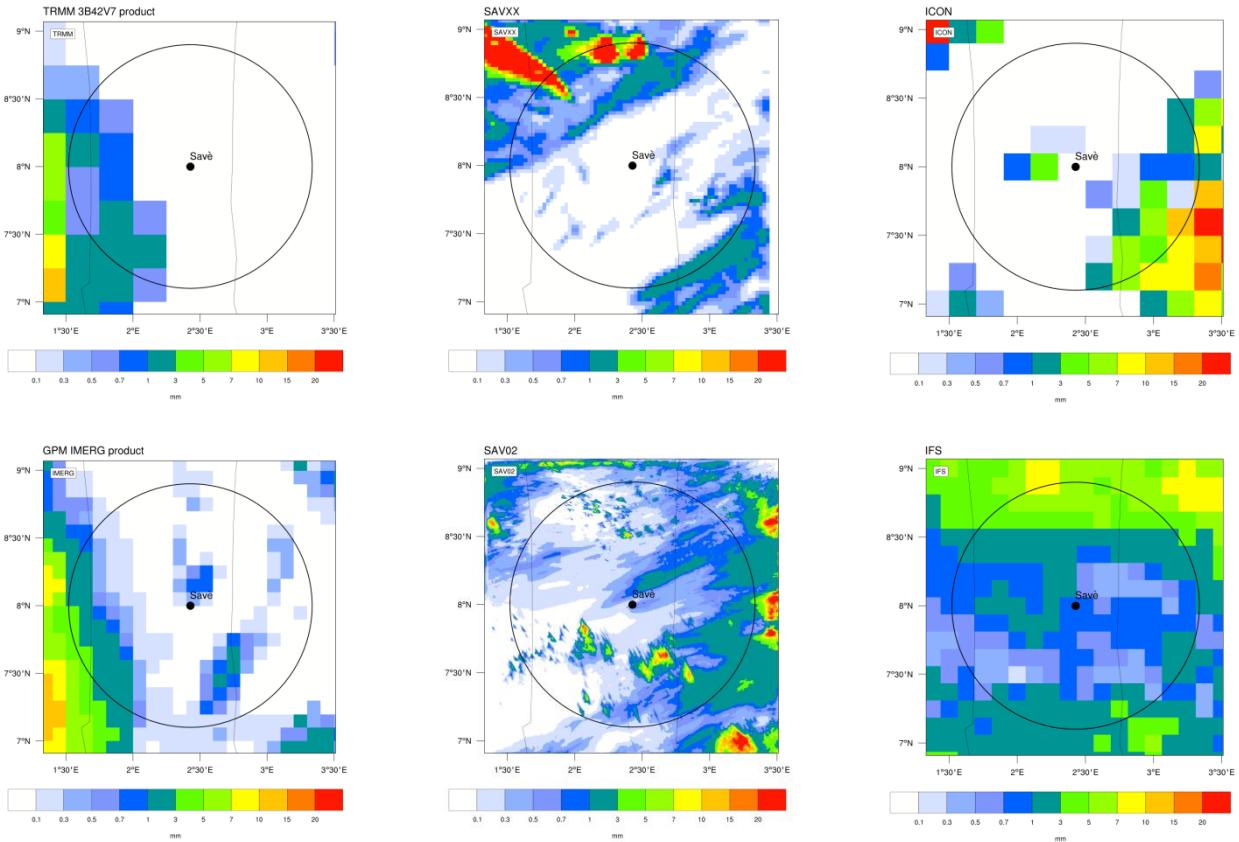
Figure 6: Accumulated rainfall from 0300 to 0900 UTC 24 July 2016 for (top left) TRMM and (bottom left) GPM, (middle) Meso-NH (top, SAVXX; bottom, SAV02), (top right) ICON and (bottom right) IFS.

Overall, the simulations give rainfall amounts in the range of the satellite retrievals, but with strong differences in location and peak values. Both Meso-NH simulations show rainfall strips in the southwest direction that mimics the GPM product. This suggests a correct sensitivity of the Meso-NH rain to the south-westerlies. They both show rainfall larger than 20 mm typical of deep convection, but in different locations. Overall, SAVXX simulates much more rainfall in the radar range than SAV02. Because of the similar grid spacing (deep convection being explicit) and model parameterization, this difference is explained by the 6-h delay in the initialization time. ICON produces rain with rather large values, which likely results from deep convection. IFS shows rainfall all over the analysis domain, but with moderate rainfall in the radar range. Note that SAVXX and IFS share the same initial conditions, but differ in the simulated rainfall. This nicely illustrates the large sensitivity of the warm rain event to the models used in this study.

5.2 Warm rain

The ability of the models to correctly simulate total rainfall and its warm rain counterpart is assessed in this section. The amount of total rainfall (for both the satellite products and the simulations) and the warm rain contribution to total rainfall (for the simulations) have been calculated from 0300 to 0900 UTC and are presented in Figure 7. No warm rain contribution is estimated for the satellite products because of the lack of data for the content of precipitating hydrometeors.

Total accumulated rainfall (mm) / Contribution to total precipitation (%)
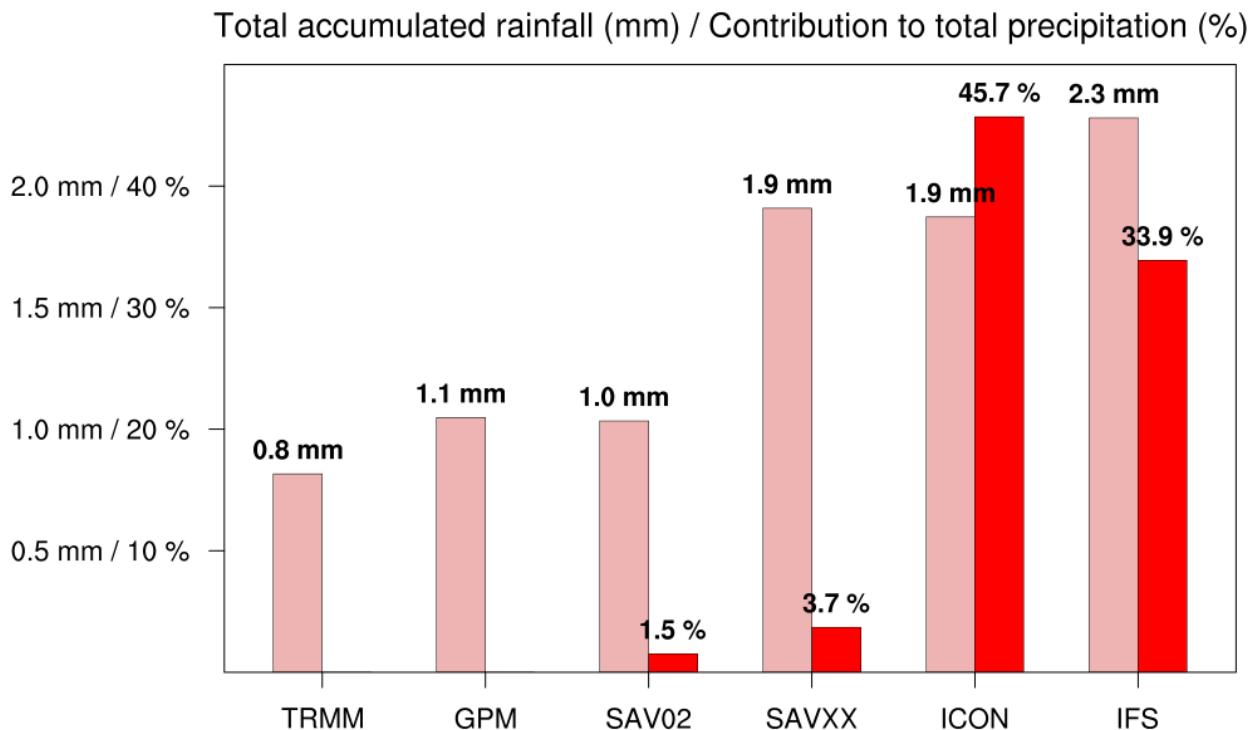
Figure 7: Histogram of accumulated rainfall from 0300 to 0900 UTC (pink bars) for TRMM, GPM, SAV02, SAVXX, ICON and IFS, and the contribution of warm rain to that amount of rainfall (red bars) for SAV02, SAVXX, ICON and IFS. The contribution is calculated every 3 h for ICON and every 1 h for the other models.

The total rainfall observed by TRMM and GPM is 0.8 and 1.1 mm, respectively. SAV02 simulates a total rainfall of 1.0 mm, similar to the observed amounts. The other simulations approximately double the value of total accumulated rainfall, giving 1.9 mm (SAVXX and ICON) and 2.3 mm (IFS). This large dispersion in the simulated rainfall is also found in the contribution of warm rain to total rainfall. The value of this contribution is 1.5, 3.7, 45.7 and 33.9 % for SAV02, SAVXX, ICON and IFS, respectively. Here the results are shown for a threshold of 0.1 g/kg on the content of precipitating hydrometeors (see Section 4) because the warm rain contribution of 1.5% for SAV02 agrees well with the climatological value of 2% obtained by Maranan et al. (2018), although these contributions must be sensitive to that threshold. The ICON and IFS contributions are the largest. The extremely large percentage obtained for ICON does not agree with the accumulated precipitation from 0300 to 0900 UTC being produced by a convective system (Figure 6). This can be due to the large errors introduced when associating instantaneous hydrometeor contents to 3-hourly accumulated rainfall to determine whether it is warm rain. In summary, the models currently show difficulties in correctly simulating the processes leading to precipitation, and particularly to warm rain.

5.3   Vertical structure of the atmosphere

To better understand the difference in simulated precipitation, we examine the vertical structure of the atmosphere. We compare the simulated fields with the radiosonde observations from Savè. The vertical profiles of potential temperature, relative humidity, wind speed and direction are shown at 0330, 0600 and 0800 UTC (Figure 8). If no model output is available at those times, the model output is taken at the closest time, that is, at 0300 UTC for SAVXX, ICON and IFS; and at 0900 UTC for ICON.

The observed potential temperature shows the static stability of the atmosphere at 0330 and 0600 UTC. At 0800 UTC, the daytime development of the boundary layer causes a neutral stratification in the first 50 hPa. All the simulations reproduce the observed potential temperature well. They however present a warm bias between 800 and 900 hPa. SAV02, that produces the smallest accumulated rainfall, also presents the largest warm bias at 0330 and 0600 UTC.

The observed relative humidity is at saturation in the lower atmosphere above 1000 hPa at 0330 and 0600 UTC. It shows several small departures from saturation at 0800 UTC. The relative humidity is overall lower in the simulations. This can be partly explained by the warm bias below the 800-hPa level. SAVXX and IFS present a similar profile at 0330 and 0600 UTC because of same initial conditions. They differ later on, at 0800 UTC. The two other simulations starting earlier present drier profiles in the lower atmosphere.

At 0330 UTC, the observed wind speed shows a maximum of more than 6 m/s at around 950 hPa with a southwesterly wind direction. This is the signature of the nocturnal low-level jet, which is reproduced by all the models with the notable exception of ICON. The latter simulates a wind speed maximum of 3 m/s too close to the surface and incorrectly superimposed by northerlies.

At 0600 UTC, south-westerlies of around 6 m/s are observed between 750 and 950 hPa. This monsoon flow is reproduced by the simulations with a correct speed and the right direction, but up to the 900-hPa level only. Indeed, the simulated wind exhibits a wrong north-westerly direction between 900 and 750 hPa (850 for ICON). Above the 750-hPa level, the simulations capture the right easterly direction of the wind, but with a too small speed.

At 0800 UTC, the wind speed has decreased to less than 4 m/s below the 800 hPa level. This observation is overall well captured by the simulations. However, the wind turns from north-westerly to south-westerly between 975 and 800 hPa. This is roughly simulated by ICON. In contrast, the three other simulations show a wrong veering from south-westerly to north-westerly. This similarity between SAV02, SAVXX and IFS suggests a large influence of synoptic-scale winds predicted by IFS and imposed at the boundary conditions of the Meso-NH simulations.

Overall, the stable moist atmosphere at Savè is well captured by the simulations, but with a small warm bias. The most notable discrepancy between observations and simulations is on the wind direction and speed, though to a lesser degree. The wind direction is of importance for organizing the cloud structure.
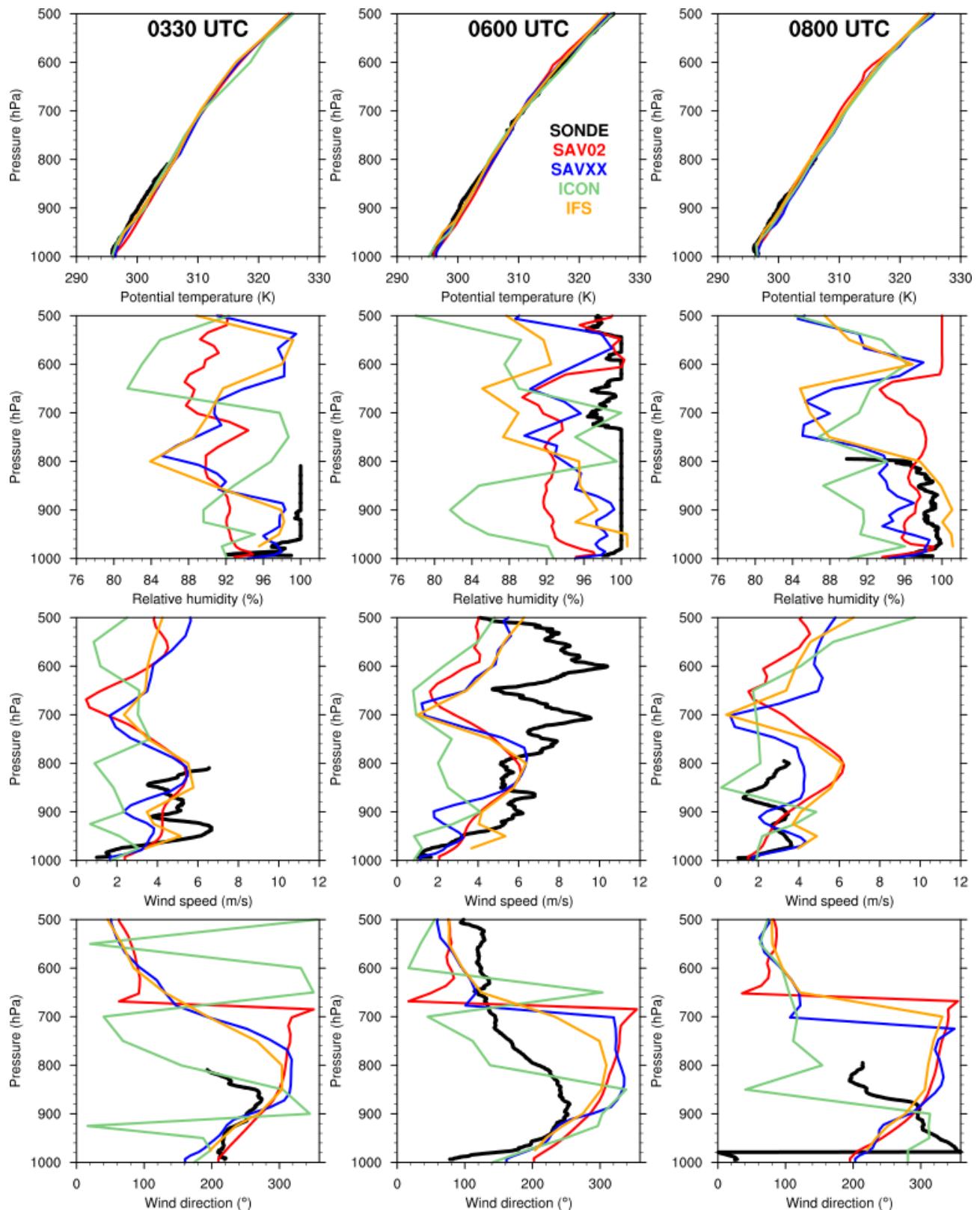
Figure 8: *Vertical profiles of, from top to bottom: potential temperature, relative humidity, wind speed and wind direction at 0330 (left), 0600 (centre) and 0800 (right) UTC 24 July 2016, for the soundings at Savè and the four simulations at the nearest gridpoint to the Savè location.*

6   Results of the Meso-NH Large-Eddy Simulation

The SAV02 LES is further analyzed because its horizontal (200 m) and vertical (50–200 m) resolutions, as well as its temporal resolution (5 min) are comparable to those of the X-band radar (500 m and 5 min). The other simulations show a too coarse grid and a too low output frequency. Thus, the analysis that we perform in the following is identical for both the radar and the SAV02 LES. It is done from 0300 to 0800 UTC, when warm rain was observed in Savè.
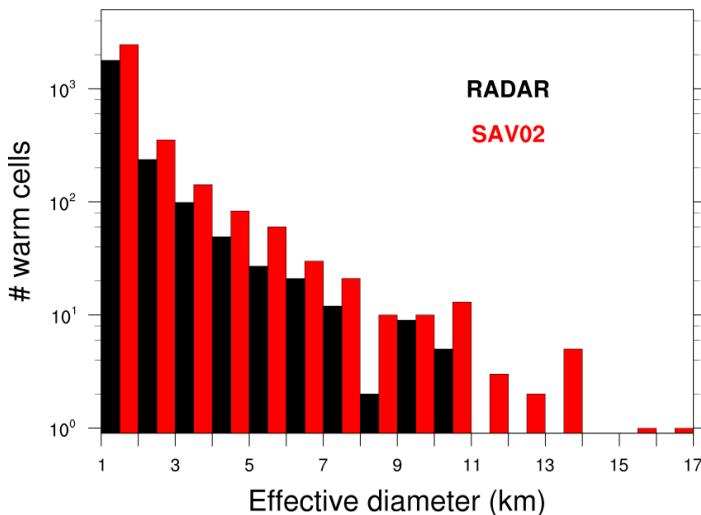
Figure 9: *Distribution of the effective diameter of the warm rain cells detected by the X-band radar (black) and simulated by the SAV02 LES (red) between 0300 and 0800 UTC. The effective diameter corresponds to the diameter of a circle occupying the same area than the warm rain cell identified with the clustering algorithm described in Section 4.*

The distribution of the effective diameter of the warm rain cells shows a decrease in the number of cells with an increasing diameter (Figure 9) for both the X-band radar and SAV02. The large majority of the warm rain cells observed by the radar (around 1500) have effective diameters ranging between 1 and 3 km. This makes them impossible to be explicitly represented by the SAVXX, ICON and IFS simulations. At the same time, the top of the warm cells being below 4-km height makes them resolved at very few vertical levels for those three simulations. On the contrary, SAV02 can represent fine atmospheric structures in more detail, such as in-cloud circulations or boundary-layer eddies leading to the triggering of warm rain cells. The five largest observed warm rain cells have diameters of 10–11 km. For the SAV02 simulation, 23 warm cells have diameters larger than 10 km. The size distribution of warm cells is thus remarkably well captured by the LES.

In Figure 10 the spatial distribution of the warm rain cells and the time when they are identified is shown for the radar and SAV02. The radar observations indicate that most of the warm cells are located west of 2º40' E. In the 50-km range around Savè, these systems are mainly seen after 0500 UTC, and those located in the 50 to 100-km range are seen earlier. Although the SAV02 simulation represents some nighttime warm cells (before 0500 UTC), as observed, it overestimates the number of warm cells after 0700 UTC. It also fails to correctly distribute the systems spatially. This failure is thought to be caused by the initial conditions.
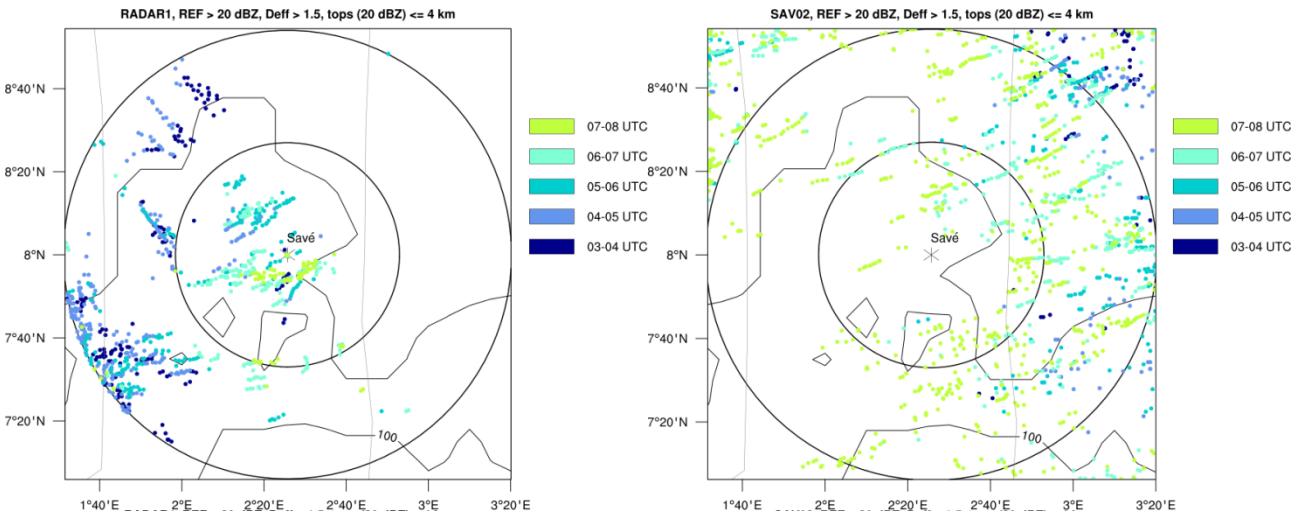
Figure 10: *Spatial distribution of the warm rain cells detected by the X-band rain radar (left) and simulated by the SAV02 LES (right) from 0300 to 0800 UTC 24 July 2016. The dots represent the location of the centre of mass of the rain cells, identified at a 5-minute temporal resolution. Only the cells with a diameter larger than 1.5 km are displayed. Colours represent the time when the rain cells are identified.*
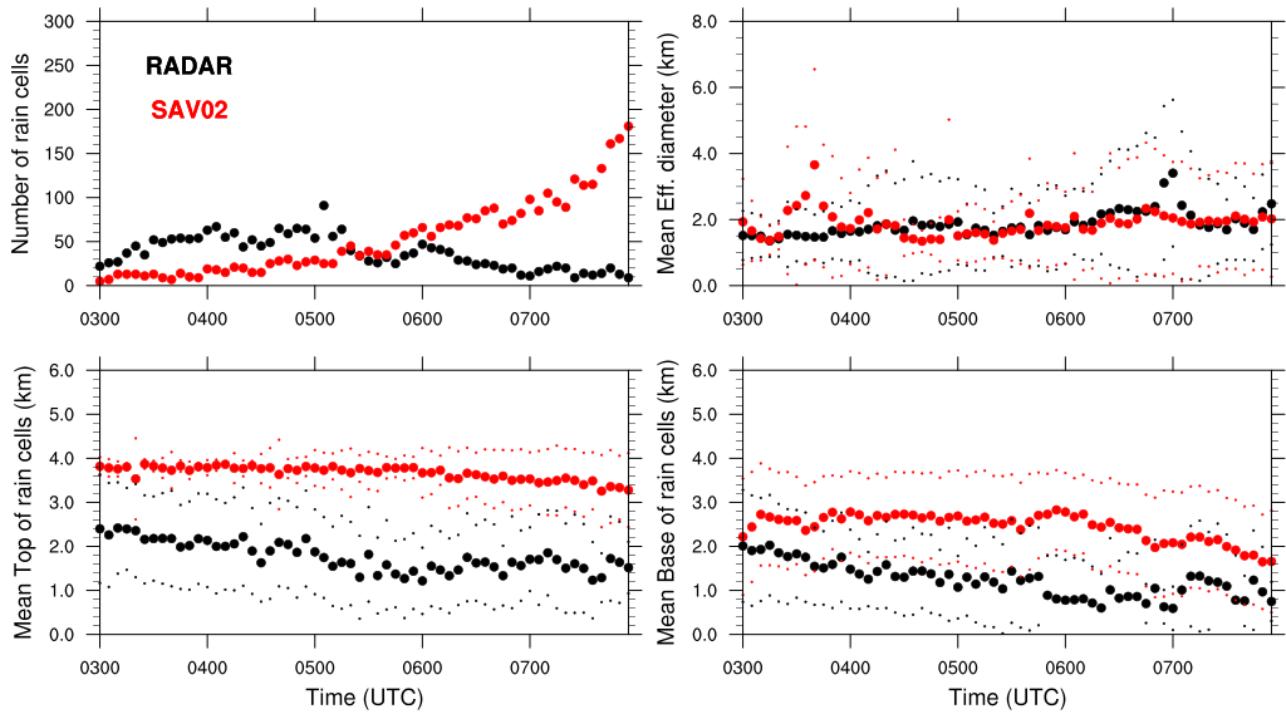
Figure 11: *Time evolution of the number (top left), and the average effective diameter (top right), top height (bottom left) and base height (bottom right) of the warm cells with diameters larger than 1.5 km, detected by the radar and SAV02 every 5 minutes. The small dots represent the standard deviation.*

The time evolution of the number and the mean values of the diameter, top and base heights of the warm rain cells are presented in Figure 11. The observed number of cells remains below 100, it slightly increases from 0300 to 0500 UTC and then decreases. The warm cells present an average effective diameter of 2 km, which remains rather constant with time. The average top (base) height decreases with time from 2.5 (2) km to 1.5 (1) km. These observed warm cells are thus 500-m deep on average. The number of cells for the SAV02 LES increases monotonically, from less than 10 cells at 0300 UTC to more than 150 at 0800 UTC. The average diameter is constant with time and around 2 km. It agrees very well with the observations during the 5-h interval. Both the simulated top and base are found higher than observed (around 1.5 and 1 km, respectively), resulting in 500-m deeper rain cells.

7 Conclusion

In this model assessment, three simulations from two research models (Meso-NH and ICON) and one operational forecast (IFS) were analyzed during the later night time and early morning of 24 July 2016 in a domain of 240 km^2 around Savè, when warm rain was observed. The simulations were evaluated against observations obtained in Savè during the DACCIWA campaign in 2016. We used radiosonde measurements of temperature, relative humidity and wind, and two satellite products for assessing precipitation. The LES run with Meso-NH was further evaluated against X-band radar-retrieved reflectivity.

The simulations show discrepancies in the spatial distribution of precipitation and total rainfall. Except for the LES, all the other simulations overestimated the total rainfall amount. ICON and IFS failed to capture the climatological contribution of warm rain to total precipitation (~2%), whereas Meso-NH performed better. The LES predicted a contribution of 1.5% which fits well with the 2% annual mean. A deficiency in the estimation of the warm rain by ICON comes from the too low frequency of model outputs. Deficiencies in the correct representation of the wind speed and direction by the models is also pointed out. Nevertheless, the short duration of this episode does not allow us to draw general conclusions about the obtained warm rain contributions. A similar analysis should be applied to longer periods in the future.

Among the possible reasons why the models struggled to represent correctly warm clouds and the associated rainfall are the model resolution and the initial conditions. A too low resolution in most of the models does not allow the updrafts and downdrafts to be explicitly represented while the errors in the wind direction and speed lead to a simulated cloud organization different to what is observed. Warm rain is a challenge even for LES. The latter captures the night-time and early-morning warm rain systems when they were observed and their size distribution, but it misses their correct spatial distribution and vertical extent (Reinares Martínez and Chaboureau, in prep.). Further analysis of the LES is needed to determine the processes driving warm rain.

8   References

Adejuwon, J. O. and T. O. Odekunle, 2006. Variability and the Severity of the "Little Dry Season" in Southwestern Nigeria. *Journal of Climate*, 19, pp 483–493

Cuxart, J., P. Bougeault, and J.-L. Redelsperger, 2000. A turbulence scheme allowing for mesoscale and large-eddy simulations. *Quarterly Journal of the Royal Meteorological Society*, 126, pp 1–30

Flamant, C., et al. 2018. The Dynamics–Aerosol–Chemistry–Cloud Interactions in West Africa Field Campaign: Overview and Research Highlights. *Bulletin of the American Meteorological Society*, 99, pp 83–104

Fouquart, Y., and B. Bonnel, 1986. Computations of solar heating of the Earth's atmosphere: A new parametrization. *Beiträge zur Atmosphärenphysik*, 53, pp 35–62

Houze, R. A., Rasmussen, K. L., Zuluaga, M. D., & Brodzik, S. R. (2015). The variable nature of convection in the tropics and subtropics: A legacy of 16 years of the Tropical Rainfall Measuring Mission satellite. *Reviews of Geophysics*, *53*(3), pp 994-1021.

Huffman, G. J., and Coauthors, 2007: The TRMM Multisatellite Precipitation Analysis (TMPA): Quasi-Global, Multiyear, Combined-Sensor Precipitation Estimates at Fine Scales. *Journal of Hydrometeorology*, 8, pp 38--55

Huffman, G. J., D. T. Bolvin, D. Braithwaite, K. Hsu, R. Joyce, C. Kidd, E. J. Nelkin, and P. Xie, 2015: NASA Global Precipitation Measurement (GPM) Integrated Multi-satellitE Retrievals for GPM (IMERG). Algorithm Theoretical Basis Doc., version 4.5, 26 pp.

Kalthoff, N. et al. 2018, An overview of the diurnal cycle of the atmospheric boundary layer during the West African monsoon season: results from the 2016 observational campaign. *Atmospheric Chemistry and Physics*, 18, pp 2913--2928

Kniffka, A., Knippertz, P., and Fink, A. H., 2018. The role of low-level clouds in the West African monsoon system, *Atmospheric Chemistry and Physics Discussion*, https://doi.org/10.5194/acp-2018-743, in review

Lac, C. et al., 2018. Overview of the Meso-NH model version 5.4 and its applications. *Geoscientific Model Development*, 11, pp 1929-1969

Machado, L. A. T., and J.-P. Chaboureau, 2015. Effect of turbulence parameterization on assessment of cloud organization. *Monthly Weather Review*, 143, pp 3246–3262

Maranan, M., A. H. Fink, and P. Knippertz, 2018. Rainfall types over southern West Africa: Objective identification, climatology and synoptic environment. *Quarterly Journal of the Royal Meteorological Society*, 144, pp 1628–1648

Masson, V., et al., 2013. The SURFEXv7.2 land and ocean surface platform for coupled or offline simulation of earth surface variables and fluxes. *Geoscientific Model Development*, 6, pp 929–960

Mlawer, E. J., S. J. Taubman, P. D. Brown, M. J. Iacono, and S. A. Clough, 1997. Radiative transfer for inhomogeneous atmospheres: RRTM, a validated correlated-k model for the longwave. *Journal of Geophysical Research: Atmospheres*, 102, pp 16 663–16 682

Mülmenstädt, J., Sourdeval, O., Delanoë, J., & Quaas, J. (2015). Frequency of occurrence of rain from liquid-, mixed-, and ice-phase clouds derived from A-Train satellite retrievals. *Geophysical Research Letters*, *42*(15), 6502-6509.

Pergaud, J., V. Masson, S. Malardel, and F. Couvreux, 2009. A parameterization of dry thermals and shallow cumuli for mesoscale numerical weather prediction. *Boundary-Layer Meteorology*, 132, pp 83–106

Pinty, J.-P., and P. Jabouille, 1998. A mixed-phase cloud parameterization for use in a mesoscale non-hydrostatic model: Simulations of a squall line and of orographic precipitation. Conference On Cloud Physics, Everett, WA, *American Meteorological Society*, pp 217–220

Reinares Martínez, I. and J.-P. Chaboureau, 2018a. Precipitation and mesoscale convective systems: explicit versus parameterised convection over Northern Africa. *Monthly Weather Review*, 146, pp 797–812

Reinares Martínez, I. and J.-P. Chaboureau, 2018b. Precipitation and mesoscale convective systems: radiative impact of dust over Northern Africa. *Monthly Weather Review*, 146, pp 3011--3029

Stein J, Richard E, Lafore JP, Pinty JP, Asencio N, Cosma S. 2000. High-resolution non-hydrostatic simulations of flash-flood episodes with grid-nesting and ice-phase parameterization. *Meteorology and Atmospheric Physics*, 72, pp 203–221

Young, M. P., Chiu, J. C., Williams, C. J., Stein, T. H., Stengel, M., Fielding, M. D., & Black, E. (2018). Spatio-temporal variability of warm rain events over southern West Africa from geostationary satellite observations for climate monitoring and model evaluation. *Quarterly Journal of the Royal Meteorological Society,* 144, pp 2311–2330